

Parameter Identification of the Lagrangian-averaged Vorticity Deviation Vortex Detection Method Through the Investigation of Fluid Flow Around Solid Bodies

Kinga Andrea Kovács¹, Esztella Balla^{1*}

¹ Department of Fluid Mechanics, Faculty of Mechanical Engineering, Budapest University of Technology and Economics, Műegyetem rkp. 3., H-1111 Budapest, Hungary

* Corresponding author, e-mail: balla.esztella@gpk.bme.hu

Received: 25 June 2023, Accepted: 18 September 2023, Published online: 10 October 2023

Abstract

The main focus of the current paper is the detection of vortices in fluid flow around a circular cylinder and a square cylinder, with an emphasis on the identification of the parameters used for vortex detection. The authors aim to enhance the practicality of an existing vortex detection method (Lagrangian-averaged vorticity deviation) by providing recommendations for the settings of the vortex detection parameters. The simulations were carried out using ANSYS Workbench 2022 R2, encompassing Reynolds numbers between 12 and 140, and angles of incidence from 0° to 45°. The vortex detection was performed using MATLAB R2020b. The paper provides a comprehensive description of the parameters involved in the detection process and their significance, as well as the implementation of the parameter identification. The study results in the determination of the suggested parameter ranges, and a comparative analysis of different vortex detection methods is also presented for the case of the circular cylinder.

Keywords

aerodynamics, bluff bodies, circular cylinder, vortex detection, parameter identification, square cylinder

1 Introduction and objectives

Extensive research has been conducted on the flow characteristics around various solid objects, driven by their wide range of practical applications. These objects are typically divided into two categories: streamlined bodies (such as airfoils) and bluff bodies (such as cylinders and spheres).

In the case of bluff bodies, within a specific range of the Reynolds number, an interesting phenomenon, known as the von Karman vortex street occurs. This phenomenon is characterized by symmetric and periodic vortex shedding [1]. The periodic nature of these flows can sometimes lead to undesirable structural vibrations. This becomes particularly dangerous when the frequency of the vortex shedding aligns with the natural frequencies of the bodies [2]. Consequently, engineers must carefully consider vortex shedding effects when designing structures such as skyscrapers and chimneys to mitigate potential risks.

Vortex shedding from streamlined bodies can be observed in the case of low-speed fans for instance. One of the most prominent noise sources of these fans originates from the so-called profile vortex shedding [3, 4]. This phenomenon

is still in the focus of current research, thus, the thorough description and understanding of it is desirable.

The primary objective of the current study is to detect vortices in fluid flow around bluff bodies, utilizing the Lagrangian-averaged vorticity deviation (LAVD) method [5]. Specifically, the investigation focuses on a circular cylinder and a square cylinder with various angles of incidence, serving as representative examples for bluff bodies. Additionally, the study includes the identification of the vortex detection parameters associated with the LAVD procedure. This is crucial as the original publication [5], which serves as the foundation for the LAVD vortex detection method, does not provide recommended values for these parameters. The current paper seeks to enhance the practicality of the LAVD vortex detection method by offering suggestions for the values of its parameters.

Vortex detection methods can be divided into two groups, local and global detection methods. Local identification methods obtain some characteristics based on the physical properties of the flow field, whereas global

methods are usually based on the global topological properties of the flow field [6].

For local detection methods (e.g., Δ -criterion, λ_2 -criterion, Q-criterion) one has to prescribe a threshold value, which makes these methods highly subjective. This threshold value is different for every case, and a recommendation for a general, optimal threshold value cannot be given. Global vortex identification methods are more objective, however, at the same time they are more computationally complex, and intensive also. The tested new detection method offers the possibility of obtaining quantitative parameters (the exact location and size) of the shed vortices. These parameters allow us to quantitatively characterize the evolved vortical structures. In addition, by using an objective vortex detection method, the process of vortex identification can be highly automatized compared to local methods.

According to [5] the definition of coherent vortices remains a subject of ongoing debate. Nevertheless, there are two key characteristics that are widely accepted. Firstly, vortices are concentrated regions exhibiting high vorticity. Secondly, they are typically perceived as evolving domains displaying a significant level of material invariance. It is important to acknowledge, however, that the precise interpretation of high vorticity lacks objectivity. Therefore, in the pursuit of establishing a clear vortex definition, material invariance can serve as a good starting point [5]. In [5] an objective vortex criterion is proposed, known as the Lagrangian-averaged vorticity deviation.

The construction of the geometry, the meshing of the flow field, and the simulations were carried out using ANSYS Workbench 2022 R2 [7]. The simulations were run for various Reynolds numbers and angles of incidence. The Reynolds number is a dimensionless value which is the ratio of the inertial forces and the viscous forces. It can be determined in the following way [1]:

$$\text{Re} = \frac{v \times \rho \times l}{\mu}, \quad (1)$$

where v is the velocity (m/s), ρ denotes the density (kg/m³), l is the characteristic length (m), and μ denotes the dynamic viscosity (kg/(m×s)). In the current paper the characteristic length for the circular cylinder is taken as the diameter of the cylinder (d), and for the square cylinder it is the projected frontal height (h).

The simulation results were validated by comparing basic flow characteristics (e.g., lift coefficient, drag coefficient, Strouhal number) with values taken from the

literature [8–10]. Furthermore, a mesh sensitivity analysis was performed to ensure that the results were independent of the grid resolution, thus, establishing the grid independence of the results.

The vortex detection was conducted using MATLAB R2020b [11]. Initially, the vortex detection and the parameter identification were carried out for the case of the circular cylinder at a Reynolds number of 120. This specific Reynolds number was chosen because it corresponds to the flow structure where vortices are periodically detached, thus, forming a von Karman vortex street [1]. For a von Karman vortex street, in the literature, there exists a theoretical value for the distance between the neighboring vortices [12]. By calculating these distances, the accuracy of the vortex detection method can be assessed, thus, providing insight into the quality of the detection method. After having found the preferred intervals of the parameters for this case, the identification was carried out for the other simulation results as well. As a final step, the vortex detection results were compared with two other methods: the instantaneous vorticity distribution and the λ_2 -criterion.

The current study can be helpful in the following practical manners. As a basic idea, through vortex detection one can observe the structure of the flow, and the effect of neighboring bodies (e.g., buildings) on one another. Moreover, vortex detection through measurements is a really time-consuming procedure, thus, the detection time can be substantially decreased by applying the current numerical method.

2 Lagrangian-averaged vorticity deviation

LAVD is defined as the integral of the normalized difference between the vorticity and its spatial mean over a trajectory [5]. Mathematically, it can be expressed as:

$$\text{LAVD}'_{t_0}(\mathbf{x}_0) = \int_{t_0}^t |\boldsymbol{\omega}(\mathbf{x}(s; \mathbf{x}_0), s) - \bar{\boldsymbol{\omega}}(s)| ds, \quad (2)$$

where t_0 is the starting time instant of the integration (s), t is the final time instant of the integration (s), \mathbf{x}_0 vector denotes the initial particle positions (m), $\boldsymbol{\omega}(\mathbf{x}, s)$ matrix is the vorticity (1/s), $\mathbf{x}(s; \mathbf{x}_0)$ matrix denotes the instantaneous particle positions (m), s is the variable of integration, and $\bar{\boldsymbol{\omega}}(s)$ vector is the instantaneous spatial mean of the vorticity (1/s).

The use of LAVD allows for the objective detection of material tubes, along which small fluid volumes exhibit the same bulk rotation compared to the mean rotation of the fluid [5]. The initial positions of these tubes correspond to tubular level surfaces of the $\text{LAVD}'_{t_0}(\mathbf{x}_0)$. In 2D, these

tubular sets can be interpreted as closed convex curves, while in 3D, they can be understood as convex, cylindrical, cup-shaped, or toroidal sets [5].

Fig. 1 [5] depicts a rotationally coherent Lagrangian vortex, showing the initial and current states on the left and right sides, respectively. $L(t)$ represents a rotational Lagrangian coherent structure, along which fluid volumes maintain the same rotation throughout the examined time interval. According to [5], a rotationally coherent Lagrangian vortex must satisfy the following conditions:

1. it is an evolving material domain $D(t)$ where $D(t_0)$ is filled with tubular level surfaces of $\text{LAVD}'_{t_0}(\mathbf{x}_0)$ and the LAVD values are decreasing as one moves outwards;
2. the boundary $B(t)$ of $D(t)$ is a material surface where $B(t_0)$ is the outermost tubular level surface (minimum) of $\text{LAVD}'_{t_0}(\mathbf{x}_0)$ in $D(t_0)$;
3. the center $C(t)$ of $D(t)$ is a material set where $C(t_0)$ is the innermost member (maximum) of $\text{LAVD}'_{t_0}(\mathbf{x}_0)$ in $D(t_0)$.

The numerical implementation and the detailed description of the LAVD method can be found in [5].

3 Simulation setup

Two-dimensional simulations were run throughout the study. Overall, four different geometries were constructed, one circular cylinder (based on [13]), and three square cylinders (based on [10]). The domain sizes differ for the circular and for the square cylinder in [10] and [13]. In order to be able to compare the simulation results with the literature data the same domain sizes were utilized as in the publications. In the case of the square cylinder, only the angle of incidence (θ) was varied with regard to the different geometries ($\theta = 0^\circ, 5^\circ, 45^\circ$). The $\theta = 0^\circ$ case is when the upper and lower boundaries of the square cylinder are parallel with the flow.

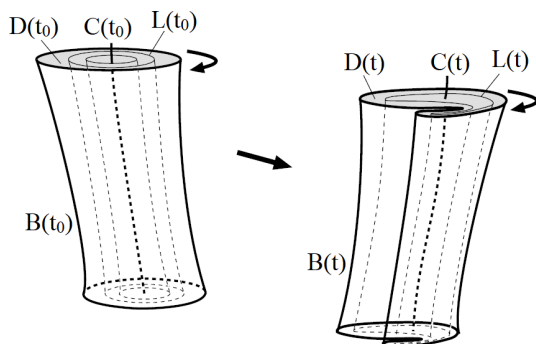


Fig. 1 Initial and current positions of a Lagrangian vortex $D(t)$; (reproduced from [5])

The diameter (d) of the circular cylinder and the side length (a) of the square cylinder have the same length: $d = a = 0.0127$ (m). As for the square cylinder, there is one additional important characteristic which is the projected frontal height (h). The projected frontal height can be calculated as follows:

$$h = a \times (\cos(\theta) + \sin(\theta)). \quad (3)$$

The geometries were constructed using SpaceClaim [7]. For the circular cylinder, the physical domain has a dimension of thirty diameters in the streamwise direction: $-8d < x < 22d$, and sixteen diameters in the lateral direction: $-8d < y < 8d$. As for the square cylinder, the simulation domain has the following parameters: $-33.5h < x < 36.5h$ and $-50h < y < 50h$.

The meshing was performed in the Ansys Workbench Mesher [7]. In each case a structured, quadrilateral mesh was generated. For the circular cylinder the smallest cell size in the domain was approximately 4×10^{-4} (m), as for the square cylinder it was 8×10^{-5} (m).

A mesh sensitivity study was also performed with the help of the Richardson extrapolation to ensure the grid independency of the results. Differently refined grids were created for two cases (circular cylinder: $\text{Re} = 120$, square cylinder: $\theta = 0^\circ$, $\text{Re} = 120$). Both for the circular and for the square cylinder, a coarse, a medium, and a fine mesh was created. For the circular cylinder, the time-averaged value of the drag coefficient, as for the square cylinder the time-averaged root mean square (RMS) value of the lift coefficient was examined. With the help of the Richardson extrapolation the discretization error was estimated:

$$\varepsilon_{h,circ} = -6.4425 \times 10^{-4}, \quad (4)$$

$$\varepsilon_{h,square} = -4.7665 \times 10^{-3}. \quad (5)$$

Another sensitivity study was carried out for the circular and the square cylinder geometry, involving the vorticity. The vorticity was monitored at different locations (the time-averaged value of it was taken), and afterwards, relative, and absolute errors were calculated between the coarse – fine and medium – fine mesh results. The relative errors were mostly below 10%, in the case of the single higher values, the absolute error was not significant compared to the maximum vorticity values occurring in the computational domain.

After the sensitivity studies, appropriately refined grids were chosen (circular: coarse grid, square: medium grid), so that the simulations would produce accurate results.

In Fig. 2 the generated local mesh can be seen with regard to the circular cylinder geometry, and in Fig. 3 the local mesh can be seen in the case of the square cylinder with a 0° angle of incidence.

The simulations were run for various Reynolds numbers using Ansys Fluent 2022 R2 [7]. The authors aimed to obtain distinct flow patterns by choosing appropriate Reynolds numbers. In the case of the circular cylinder the chosen Reynolds numbers were based on the findings in [8], and for the square cylinder the chosen Reynolds numbers and angles of incidence were based on [10]. The aim was to visualize basic flow patterns while staying in the laminar flow regime, for the circular cylinder these are the following [8]: steady, symmetric separation; laminar, unstable wake; von Karman vortex street. In [10] it is stated that in the case of a square cylinder there are three main distinct flow patterns in the laminar regime: main separation (MS) (which has two subpatterns: single secondary vortex (SSV), and dual secondary vortices (DSVs)), vortex

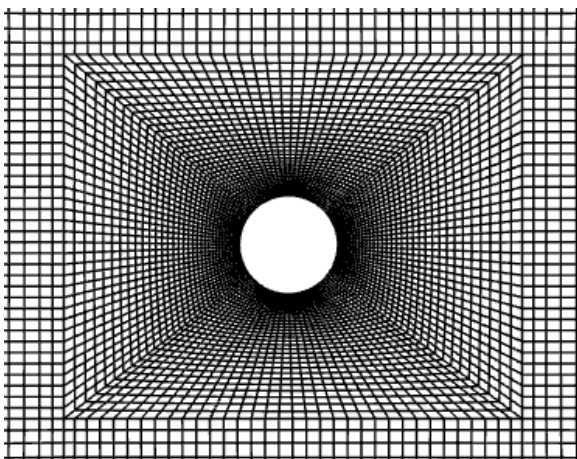


Fig. 2 The local mesh for the circular cylinder

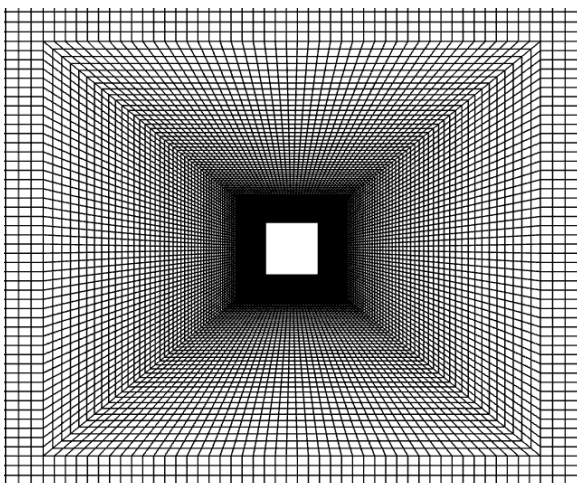


Fig. 3 The local mesh for the square cylinder ($\theta = 0^\circ$)

merging (VM), and steady (S). The investigated cases can be seen in Table 1. The appropriate time step values were determined based on the definition of the Courant number.

The simulations were run using the Viscous Laminar model and applying second-order numerical schemes.

The boundary conditions were set based on [13], and they are identical in each simulation case. For the inlet and the outlet a velocity inlet, and a pressure outlet boundary condition were prescribed, respectively. For the upper and lower boundaries symmetry boundary condition was set. The wall of the cylinder was specified as no-slip wall in order to bound fluid and solid regions. The applied boundary conditions can be seen in Fig. 4.

4 Results and discussion

4.1 Validation of the simulations

In the case of the circular cylinder, different flow behaviors were observed at different Reynolds numbers. At a Reynolds number of 12 steady symmetric separation, and for a Reynolds number of 60 a laminar unstable wake could be observed. When the Reynolds number increased to 120, symmetric periodic vortex shedding occurred, commonly known as the von Karman vortex street phenomenon. These findings align with the expectations documented in the literature [8, 9]. As an illustrative example, Fig. 5 shows the contour plot of the velocity at a Reynolds number of 120.

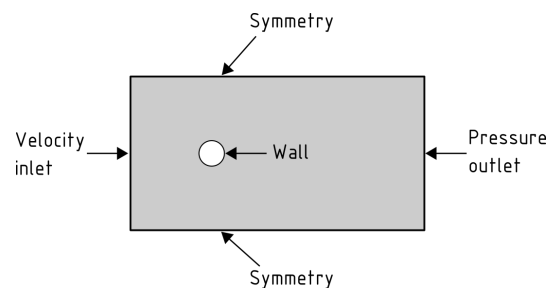


Fig. 4 The applied boundary conditions (figure not to scale)

Table 1 The investigated simulation cases

Cylinder type	Angle of incidence	Reynolds number	Time step size (s)
Circular	–	12	Steady
		60	0.005
		120	0.002
Square	0°	40	Steady
		100	0.0007
		140	0.0005
		100	0.0007
	5°	100	0.0007
	45°	120	0.0008

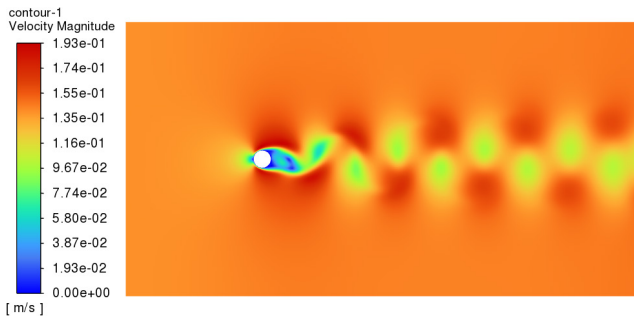


Fig. 5 Contour plot of velocity at $Re = 120$

As it was already mentioned, for the square cylinder the angle of incidence and Reynolds number pairings were chosen based on [10]. The occurrence of the flow patterns which were already mentioned (MS, SSV, DSVs, VM, S) varies with the Reynolds number, and the angle of incidence. The aim was to visualize these distinct flow patterns. The simulation results revealed that the observed flow patterns aligned with the anticipated outcomes. A representative example can be seen in Fig. 6 with regard to the vortex merging pattern ($\theta = 45^\circ$, $Re = 120$).

Apart from the flow structure (for the validation of the simulation results), different flow characteristics were examined. The flow characteristics under examination were the following: time-averaged lift and drag coefficient, and the Strouhal number. The simulation results (subscript: *sim*) for the different cases, as well as the values taken from the literature [8–10] (subscript: *lit*) can be seen in Tables 2 and 3. There are some cases when the Strouhal number is not presented, this applies for steady cases of fluid flow. For stationary flows vortex shedding is not observable, thus, the Strouhal number (which depends on the vortex shedding frequency) is not defined.

In the case of a symmetric flow the time-averaged value of the lift coefficient is zero. One can see that this has been fulfilled in each symmetric case. As for the obtained drag coefficients, and Strouhal numbers, these are also in accordance with the expected results.

4.2 Vortex detection

As stated in the introduction, the initial focus of the study involved vortex detection and parameter identification for the case of the circular cylinder at a Reynolds number of 120. This choice was driven by the presence of a theoretical value for the ratio of the coordinate differences between neighboring vortices for a von Karman vortex street [12], this value is 0.281.

Referring back to Eq. (2), it is required to set the temporal length of the integration. The LAVD method is able

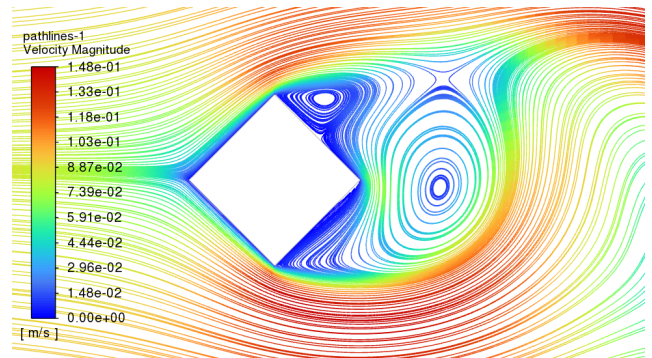


Fig. 6 Pathlines for the vortex merging pattern ($\theta = 45^\circ$, $Re = 120$)

Table 2 Simulation results for the circular cylinder

Re [-]	$\bar{c}_{L,sim}$ [-]	$\bar{c}_{L,lit}$ [-]	$\bar{c}_{D,sim}$ [-]	$\bar{c}_{D,lit}$ [-]	Sr_{sim} [-]	Sr_{lit} [-]
12	0	0	2.81	2.53	–	–
60	0	0	1.49	1.38	0.14	0.14
120	0	0	1.40	1.31	0.18	0.17

Table 3 Simulation results for the square cylinder

θ [°]	Re [-]	$\bar{c}_{L,sim}$ [-]	$\bar{c}_{L,lit}$ [-]	$\bar{c}_{D,sim}$ [-]	$\bar{c}_{D,lit}$ [-]	Sr_{sim} [-]	Sr_{lit} [-]
	40	0	0	1.68	1.66	–	–
0°	100	0	0	1.48	1.43	0.14	0.14
	140	0	0	1.48	1.40	0.15	0.16
5°	100	-0.04	-0.02	1.41	1.38	0.15	0.15
	120	0	0	1.84	1.76	0.18	0.18

to detect vortices from a minimum of two time steps. By increasing the integration time, the accuracy of the vortex detection also increases. However, the integration time is bounded by the size of the domain, since above a certain maximal integration time the fluid particles leave the computational domain, and the LAVD values cannot be interpreted. According to our investigations, between the minimum and maximum integration time there is a time range in which the result of the method is not sensitive to the change in the integration time. The integration times were selected within this range so that the fluid would cover approximately the same path in each case (separately for the circular and the square cylinder).

The identification was performed for the following three vortex detection parameters: *Nct*, *DeficiencyThresh* (%), *MinLength* (%). *Nct* denotes the number of LAVD contour levels intended to extract. The *DeficiencyThresh* parameter is the maximum allowable convexity deficiency of the detectable vortices. The convexity deficiency of a closed curve in the plane is defined as the ratio of the area between the curve and its convex hull to the area enclosed by the curve [5]. At last, the *MinLength* parameter is the minimum

required perimeter of a vortex. If the perimeter of a given vortex falls below this threshold value, then it is going to be omitted. It is also important to note, that *MinLength* is expressed as a percentage of the cylinder diameter and the projected frontal height for the circular cylinder, and the square cylinder, respectively. Meaning, if *MinLength* is set to 20%, then the minimum required perimeter of a vortex is 20% of the diameter/projected frontal height.

At the beginning of the identification procedure the effect of the *Nct* parameter was examined, while keeping the other two parameters at a constant value. Afterwards, with a chosen preferred value for *Nct* the identification was performed for the other two parameters as well.

During the parameter identification the tested values were the following: *Nct* = 1, 10, 50, 100, 200, 400, 600, 800, 1000; *DeficiencyThresh* = 0, 1, 2, 5, 10, 15, 20, 40, 50, 60, 80, 100%; *MinLength* = 1, 10, 20, 40, 60, 65, 70, 75, 80, 100, 110, 120, 130, 150, 180, 185, 190, 200, 1000%.

The identification was carried out through the visual inspection of the results. It was vital that there would be no detected vortices before the cylinder. In addition, the parameter values were chosen so that a complete vortex row would be detected.

The suggested intervals were determined for each parameter, these are the following: *Nct* ∈ [100; 200]; *DeficiencyThresh* ∈ [1; 10]%; *MinLength* ∈ [75; 180]%. Within these intervals, the obtainable vortex detection results are in great accordance with each other. After having finished the identification process, the vortex detection with preferred parameter values was performed, and the realization of the theoretical 0.281 value was also inspected. The outcome of the vortex detection can be seen in Fig. 7, which is the contour plot of the calculated LAVD values. The red dots denote the centers, and the red, closed curves denote the boundaries of the vortices. Given that two-dimensional simulations were conducted, the applied reference system is the *x-y* coordinate system, with the origin positioned at the center of the cylinder.

After calculating the ratios of the coordinate differences between the neighboring vortices, the following results were received:

$$\begin{aligned} \frac{\Delta y_{12}}{\Delta x_{12}} &= 0.4038, & \frac{\Delta y_{23}}{\Delta x_{23}} &= -0.3409, \\ \frac{\Delta y_{34}}{\Delta x_{34}} &= 0.3063, & \frac{\Delta y_{45}}{\Delta x_{45}} &= -0.2804, \\ \frac{\Delta y_{56}}{\Delta x_{56}} &= 0.2844. \end{aligned} \tag{6}$$

From Eq. (6), it is evident that the calculated values closely approximate the conceptual value. Moreover, as the flow progresses downstream from the cylinder, these calculated values converge towards the theoretical value.

Afterwards, the parameter identification was performed for the other simulation results as well. As a representative example, in Fig. 8 one can see the result of the vortex detection for the square cylinder with $\theta = 45^\circ$ at $Re = 120$. The detection was not successful for two of the cases: circular cylinder at $Re = 12$, and square cylinder with $\theta = 0^\circ$ at $Re = 40$. The unsuccessful vortex detection is a result of the fact that in these cases the flow is steady, thus, the vortices are at a fixed place, they are not shed.

The determined intervals, and their sections for every examined case are summarized in Tables 4 and 5. One can see that though the suggested intervals are not exactly the same for every case, each parameter has values which are appropriate for all of the cases. It is also important to note, that the value of *MinLength* is in accordance with the cylinder diameter/projected frontal height, this is why it was

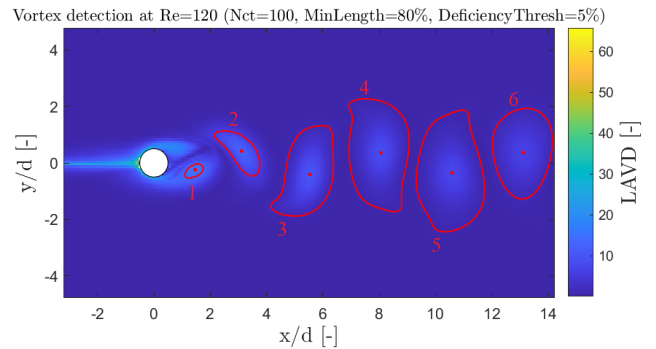


Fig. 7 Vortex detection with suggested parameters at $Re = 120$

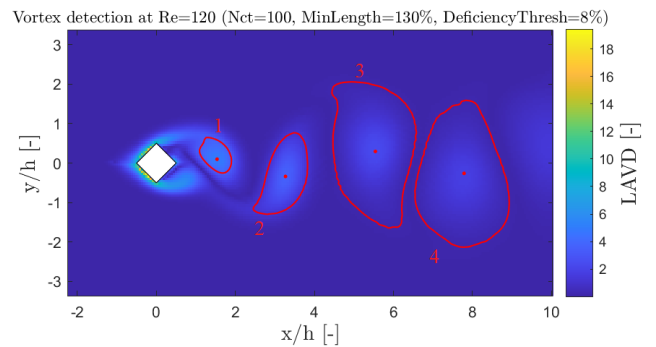


Fig. 8 Vortex detection with suggested parameters at $\theta = 45^\circ$, $Re = 120$

Table 4 Summary of the suggested intervals for the circular cylinder

	$Re = 60$	$Re = 120$	\cap
<i>Nct</i> [-]	[100; 200]	[100; 200]	[100; 200]
<i>DeficiencyThresh</i> [%]	[1; 10]	[1; 10]	[1; 10]
<i>MinLength</i> [%]	[60; 495]	[75; 180]	[75; 180]

Table 5 Summary of the suggested intervals for the square cylinder

	$\theta = 0^\circ$ and $Re = 100$	$\theta = 0^\circ$ and $Re = 140$	$\theta = 5^\circ$ and $Re = 100$	$\theta = 45^\circ$ and $Re = 120$	\cap
<i>Nct</i> [-]	[100; 200]	[100; 200]	[100; 150]	[100; 200]	[100; 150]
<i>DeficiencyThresh</i> [%]	[6; 10]	[5; 10]	[5; 10]	[1; 10]	[6; 10]
<i>MinLength</i> [%]	[80; 145]	[60; 135]	[110; 125]	[95; 260]	[110; 125]

beneficial to express *MinLength* as a percentage of these characteristic values.

Furthermore, the ratios of the coordinate differences for each examined case were also determined. Starting with the circular cylinder, the ratios for $Re = 60$ were determined (this can be seen in Eq. (7)), and a few deductions were made.

$$\begin{aligned} \frac{\Delta y_{12}}{\Delta x_{12}} &= -0.4922, & \frac{\Delta y_{23}}{\Delta x_{23}} &= 0.4738, \\ \frac{\Delta y_{34}}{\Delta x_{34}} &= -0.4938. \end{aligned} \tag{7}$$

For a Reynolds number of 60, Eq. (7) demonstrates that the vortex shedding exhibits symmetry, with alternating positive and negative signs in the ratios, and the absolute values of the ratios being relatively similar. However, unlike the $Re = 120$ scenario, the ratios do not converge but rather immediately become uniform (the 0.281 theoretical value is not valid for this case, since it only holds for a von Karman vortex street).

With respect to the square cylinder, the theoretical 0.281 value was realized in almost all of the examined cases. The only exception was the $\theta = 0^\circ$, $Re = 140$ case. This occurrence might be due to the fact that in this case the Reynolds number is close to the critical value above which the flow transitions to three-dimensional [10, 14]. If this occurs a two-dimensional simulation cannot capture the effect of three-dimensional structures on the flow field, and this explains why the 0.281 criterion was not met.

4.3 Comparison of different vortex detection methods

As it has already been mentioned, the literature is still lacking an exact vortex definition. Consequently, there exists a vast number of different vortex detection methods, and there is no general agreement with respect to which of these methods is the best.

In the upcoming paragraphs the detection results obtained with methods other than the LAVD will be presented, these methods are the following: instantaneous vorticity distribution, and the λ_2 -criterion. The vortex detection was performed for the circular cylinder case at a Reynolds number of 120. The comparison of the results

is conducted by calculating the differences of the coordinates of the detected vortex centers (only those vortices are considered which have been found by each method).

The first applied method is based on the instantaneous vorticity distribution. The vorticity data from Fluent was exported for a given time instant (which is the starting time instant of the integration in the LAVD method) and the vortex detection was performed by finding local maxima in MATLAB. As it was mentioned beforehand, a threshold value has to be prescribed, which was based mostly on the visual inspection of the results. This value is the following: $\omega_{thresh} = 10$ (1/s), all values below ω_{thresh} were omitted from further examination. The outcome of the vortex detection based on the vorticity distribution can be seen in Fig. 9. The red dots denote the centers of the detected vortices (local maxima), and only those vortices were numbered which were found by the LAVD method as well (all in all 12 vortices were detected).

As for the second method, the λ_2 -criterion was chosen, which is also a local vortex identification criterion. The λ_2 data from Fluent was exported, and in MATLAB the vortex identification was performed by setting a threshold value, and by finding local minima. Similarly to the previous case, the threshold value was set based on visual inspection, and it is the following: $\lambda_{2,thresh} = -35$ ($1/s^2$), all values above $\lambda_{2,thresh}$ were omitted from further examination. The vortex detection based on the λ_2 -criterion can be seen in Fig. 10. The same things apply as for the previous case, the red dots denote the centers of the detected vortices, and only those vortices were numbered which were found by the LAVD method too (all in all 9 vortices were detected).

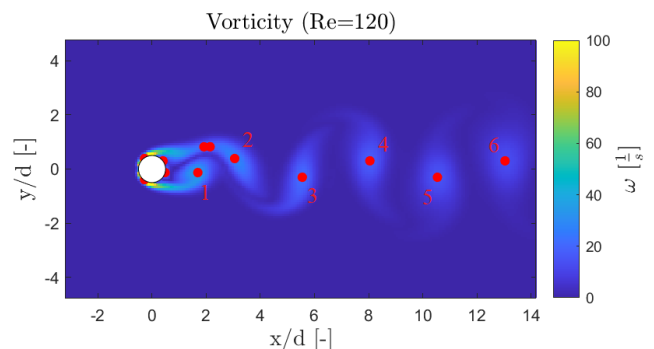


Fig. 9 Vortex detection based on vorticity

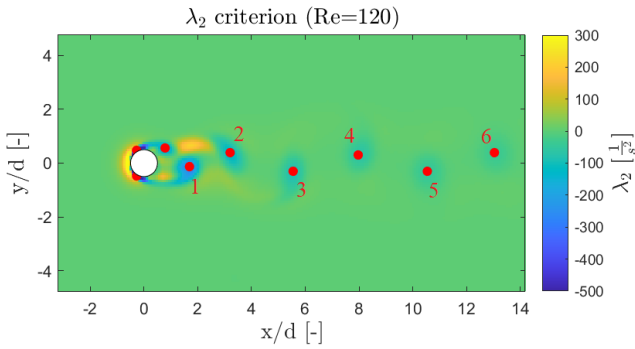


Fig. 10 Vortex detection based on the λ_2 -criterion

After performing the detection with these other two methods as well, coordinates of the centers of the vortices were exported, and the absolute differences were determined with respect to the LAVD results, and also between the vorticity and λ_2 results. This can be seen in Table 6.

It can be seen from Table 6 that the absolute differences in the x and y directions are not significant (it falls within the order of magnitude of the mesh size), especially in the case of vortices further down in the cylinder's wake. However, it can be seen from Figs. 9 and 10 that the number of detected vortices is higher than in the case of the LAVD method. Some of these vortices are artificial vortices (e.g., vortices in front of the cylinder) which can be a result of numerical noise in the velocity data. Partly, this is why the LAVD method is a better solution, because through the adjustable parameters these occurrences can be eliminated. In addition, the required convexity can also be ensured by setting the *DeficiencyThresh* parameter to an appropriate value, thus, also considering the shape of the vortices. On the other hand, it is much easier to implement the presented local detection methods, and the computational cost is also relatively low compared to the LAVD.

5 Summary of results

The main aim of the study was the parameter identification of an existing vortex detection method, and the detection of the evolved vortices in fluid flow around a circular cylinder and a square cylinder.

The identification was at first performed for the circular cylinder geometry at $Re = 120$. After performing the detection with the preferred parameters, the calculated distances between the neighboring vortices were close to the theoretical value characteristic of the von Karman vortex street. The identification was performed for the other cases as well, and except for the steady case of fluid flow ($Re = 12$), it was successful. As for the square cylinder, the identification was also successfully performed, except for the stationary case ($\theta = 0^\circ$, $Re = 40$). For the *Nct* and *MinLength* parameters, there is a common section with respect to the two geometries, these are the following: $Nct \in [100; 150]$, $MinLength \in [110; 125]\%$. As for the convexity deficiency threshold, it is advisable to set a *DeficiencyThresh* between 1% and 10% of the characteristic size of the investigated body. Further tuning within this range may be required to obtain appropriate results for the vortex detection.

The vortex detection results obtained with the (global) LAVD method were compared with other (local) vortex detection results. The applied additional vortex identification methods were the following: detection based on the instantaneous vorticity distribution, and detection based on the λ_2 -criterion. The comparison was performed by determining the absolute differences between the coordinates of the centers of the detected vortices. Even though the differences were insignificantly small, it was also deduced that these local methods detected artificial vortices, which can be eliminated by the application of the LAVD method. Moreover, with the help of the LAVD method the required convexity can also be set. On the other hand, the implementation of the local detection methods is easier than that of the LAVD method, and the computational cost is also lower while applying local detection methods.

In conclusion, the parameter identification of the LAVD vortex detection method has successfully been carried out within the study. By providing the suggested values for the vortex detection parameters, the usage of the LAVD method has been made easier. Through the comparison

Table 6 Comparison of the different vortex detection results

Serial number	Absolute difference LAVD (Vorticity)		Absolute difference LAVD (λ_2)		Absolute difference (Vorticity - λ_2)	
	$ \Delta x$ [m]]	$ \Delta y$ [m]]	$ \Delta x$ [m]]	$ \Delta y$ [m]]	$ \Delta x$ [m]]	$ \Delta y$ [m]]
1	0.0028	0.0014	0.0028	0.0014	0	0
2	0.0007	0.0003	0.0012	0.0003	0.0019	0
3	0.0002	0.0013	0.0002	0.0013	0	0
4	0.0001	0.0007	0.0011	0.0007	0.0010	0
5	0.0005	0.0006	0.0005	0.0006	0	0
6	0.0009	0.0008	0.0009	0.0003	0	0.0011

with other detection methods, the advantages, and the disadvantages could be observed of each method (LAVD: accurate, the preferred vortex shape can be set, but also time-consuming and it is harder to implement; vorticity, λ_2 -criterion: less accurate, the vortex shape cannot be regulated, but relatively fast, and easy to implement). However, further work is needed to perform the identification for more cases (e.g., three-dimensional simulations, other geometries), and to compare the suggested parameter values for the different setups. These studies would offer further possibilities for the evaluation of the LAVD method's performance against other methods.

Acknowledgement

Project no. 143204 has been implemented with the support provided by the Ministry of Innovation and Technology of Hungary from the National Research, Development and Innovation Fund, financed under the OTKA K 22 funding scheme. Project no. TKP-6-6/PALY-2021 has been implemented with the support provided by the Ministry of Culture and Innovation of Hungary from the National Research, Development and Innovation Fund, financed under the TKP2021-NVA funding scheme.

Nomenclature

Latin letters	Name	Unit
a	Side length	m
$B(t)$	Boundary of a rotationally coherent Lagrangian vortex	–
c_D	Drag coefficient	1
c_L	Lift coefficient	1
$C(t)$	Center of a rotationally coherent Lagrangian vortex	–
d	Diameter	m
$D(t)$	Rotationally coherent Lagrangian vortex	–
h	Projected frontal height	m
l	Characteristic length	m
$L(t)$	Lagrangian coherent structure	–
Re	Reynolds number	1

s	Variable of integration	–
Sr	Strouhal number	1
t	Final time instant of the integration	s
t_0	Starting time instant of the integration	s
v	Velocity	$m \times s^{-1}$
$\mathbf{x}(t, \mathbf{x}_0)$	Instantaneous particle positions	m
\mathbf{x}_0	Initial particle positions	m
$ \Delta x $	Absolute difference in the x -direction	m
$ \Delta y $	Absolute difference in the y -direction	m

Greek letters	Name	Unit
ε_h	Discretization error	1
θ	Angle of incidence	°
μ	Dynamic viscosity	$kg \times m^{-1} \times s^{-1}$
ρ	Density	$kg \times m^{-3}$
$\omega(\mathbf{x}, t)$	Vorticity	s^{-1}
$\bar{\omega}(t)$	Instantaneous spatial mean of the vorticity	s^{-1}

Abbreviations

<i>DeficiencyThresh</i>	Convexity deficiency threshold
DSVs	Dual secondary vortices
LAVD	Lagrangian-averaged vorticity deviation
<i>MinLength</i>	Minimal arc-length threshold
MS	Main separation
<i>Nct</i>	Number of contour levels
S	Steady
SSV	Single secondary vortex
VM	Vortex merging

References

- [1] Anderson, J. "Fundamentals of Aerodynamics", McGraw Hill, 2017. ISBN 978-1259129919
- [2] Irwin, P. A. "Vortices and tall buildings: A recipe for resonance", *Physics Today*, 63(9), pp. 68–69, 2010.
<https://doi.org/10.1063/1.3490510>
- [3] Daku, G., Vad, J. "Profile vortex shedding from low-speed axial fan rotor blades: a modelling overview", *Proceedings of the Institution of Mechanical Engineers, Part A: Journal of Power and Energy*, 236(2), pp. 349–363, 2022.
<https://doi.org/10.1177/09576509211026821>
- [4] Balla, E., Vad, J. "Refinement of a Semi-Empirical Method for the Estimation of Profile Vortex Shedding Frequency from Low-Speed Axial Fan Blade Sections", In: *14th European Conference on Turbomachinery Fluid dynamics & Thermodynamics*, Gdansk, Poland, 2021, ETC2021-591. ISBN 2410-4833
<https://doi.org/10.29008/ETC2021-591>
- [5] Haller, G., Hadjighasem, A., Farazmand, M., Huhn, F. "Defining coherent vortices objectively from the vorticity", *Journal of Fluid Mechanics*, 795, pp. 136–173, 2016.
<https://doi.org/10.1017/jfm.2016.151>
- [6] Wang, J., Guo, L., Wang, Y., Deng, L., Wang, F., Li, T. "A Vortex Identification Method Based on Extreme Learning Machine", *International Journal of Aerospace Engineering*, 2020, 8865001, 2020.
<https://doi.org/10.1155/2020/8865001>
- [7] Ansys "Ansys Workbench, (22.2)", [computer program] Available at: <https://www.ansys.com/academic/students/ansys-student> [Accessed: 10 March 2022]
- [8] Schlichting, H., Gersten, K. "Boundary-Layer Theory", Springer, 2017. ISBN 978-3-662-52917-1
<https://doi.org/10.1007/978-3-662-52919-5>
- [9] Qu, L., Norberg, C., Davidson, L., Peng, S.-H., Wang, F. "Quantitative numerical analysis of flow past a circular cylinder at Reynolds number between 50 and 200", *Journal of Fluids and Structures*, 39, pp. 347–370, 2013.
<https://doi.org/10.1016/j.jfluidstructs.2013.02.007>
- [10] Yoon, D.-H., Yang, K.-S., Choi, C.-B. "Flow past a square cylinder with an angle of incidence", *Physics of Fluids*, 22(4), 043603, 2010.
<https://doi.org/10.1063/1.3388857>
- [11] The MathWorks "MATLAB, (9.9)", [computer program] Available at: https://www.mathworks.com/products/new_products/release_2020b.html [Accessed: 16 November 2020]
- [12] Glauert, H. "The Elements of Aerofoil and Airscrew Theory", Cambridge University Press, 1983. ISBN 9780511574481
<https://doi.org/10.1017/CBO9780511574481>
- [13] Shao, J., Zhang, C. "Numerical analysis of the flow around a circular cylinder using RANS and LES", *International Journal of Computational Fluid Dynamics*, 20(5), pp. 301–307, 2006.
<https://doi.org/10.1080/10618560600898437>
- [14] Sheard, G. J., Fitzgerald, M. J., Ryan, K. "Cylinders with square cross-section: Wake instabilities with incidence angle variation", *Journal of Fluid Mechanics*, 630, pp. 43–69, 2009.
<https://doi.org/10.1017/S0022112009006879>